Kovove Mater. 63 2025 157–168 DOI: <u>10.31577/km.2025.3.157</u>

Impact of additive elements on the structural, thermal, and magnetic properties of arc-melted Ni-Si-M (M = Al, Cu, Zr) ternary alloys

Sinan Diken¹*, Celal Kursun², Musa Gogebakan²

¹Department of Physics, Faculty of Science, Kilis 7 Aralık University, Kilis 79000, Turkey
²Department of Physics, Faculty of Art and Sciences, Kahramanmaraş Sütçü İmam University, Kahramanmaras 46100,
Turkey

Received 13 May 2025, received in revised form 5 August 2025, accepted 5 September 2025

Abstract

This work investigates the effects of additive elements on the microstructural evolution, thermal transformation, morphological and magnetic properties of Ni-Si-rich (Ni₈₀Si₂₀)₉₅M₅ (M = Al, Cu, Zr) ternary alloys. The alloys were manufactured by conventional solidification using an arc-melting system under a vacuum atmosphere. Systematic characterizations were carried out through a combined study of X-ray diffraction (XRD), differential thermal analysis (DTA), differential scanning calorimetry (DSC), scanning electron microscopy with energy-dispersive X-ray spectroscopy (SEM-EDX), Vickers micro-hardness tester, and vibrating sample magnetometry (VSM). XRD analysis detected the presence of β_1 -Ni₃Si and γ -Ni₃₁Si₁₂ phases, revealing variations in peak intensities and crystallite sizes among the alloys, influenced by the third alloying element.

Both the XRD and SEM-EDX results confirm that the alloys consist of the intermetallic phases and exhibit compositional homogeneity, with measured values closely matching the nominal compositions. DSC indicated thermal stability between 60–680 °C for all alloys, while DTA traces displayed single or double endothermic peaks between 1074 and 1197 °C. Vickers micro-hardness measurements revealed distinct differences among the $(Ni_{80}Si_{20})_{95}M_5$ alloys, with values of 613.4, 823, and 882.4 HV for M=Al, Cu, and Zr, respectively, highlighting the strengthening effect of the alloying elements. Magnetic properties such as the remanent magnetization (M_r) and the coercive field (H_c) were calculated from the hysteresis loops, and the results are thoroughly discussed. This work provides meaningful insights for designing, improving, and controlling the parameters of the new Ni-Si-rich ternary alloys with desired properties.

 $\rm K~e~y~w~o~r~d~s:$ arc melting, Ni-Si based alloys, ternary alloys, microstructure, magnetic properties, minor alloying

1. Introduction

Metals are indispensable constituents of many commercial and conventional alloys with their unique combinations of mechanical, microstructural, magnetic, and thermophysical properties [1, 2]. In particular, nickel-based alloys are fundamental to high-temperature components like turbine blades, turbine disks, and rocket engines in aviation and electric industries [3], while also serving as structural materials in nuclear reactors [4–8]. Additionally, these alloys find

application areas in dentistry [9, 10] and the petrochemical industries [11]. Therefore, in recent years, Ni-based alloys have been the focus of intense research efforts to exploit their characteristic properties. Suryanarayana et al. synthesized NiSi and NiSi₂ compounds using mechanical alloying (MA) and reported that formation of a homogeneous NiSi₂ phase could be obtained only when the initial Si content was at least about 75 % [12]. Omuro and Miura also investigated Ni-Si powder blends and successfully obtained Ni₃₁Si₁₂ (γ) and Ni₂Si phases in the amorphous

^{*}Corresponding author: e-mail address: sinandiken@kilis.edu.tr

state with the help of high-energy ball milling using a revolution-steplike-decreasing (RSD) mode [13]. Electrochemical characteristics of Si-Ni alloy and graphite composites were studied by M. S. Park et al. using the arc-melting process. In their study, an increase in the electronic conductivity of the composite materials was reported due to NiSi and NiSi2 phases serving as an inactive buffer matrix [14]. Takasugi et al. found that the effect of Cr addition on mechanical and chemical properties of Ni₃Si alloys resulted in notable enhancements such as significant strengthening over a wide range of temperatures, large compressive plastic deformation at temperatures above 900 K, improved oxidation resistance in air at 1173 K and corrosion resistance compared to the Ni₃Si binary and the Ni₃(Si, Ti) alloys [15]. Boyuk et al. studied Al--Si-Ni alloy and reported that Al11.1wt.%Si4.2wt.%Ni eutectic exhibits finer eutectic structure than the binary Al-Si eutectic alloy [16]. These findings highlight the potential of Ni-Si alloys to address key challenges in energy conversion, transportation, and industrial processing applications where conventional materials often fail under extreme conditions.

The influence of microstructural factors, including phase composition and stability, grain size, grain morphology, and crystallographic texture, is widely acknowledged as a fundamental factor shaping the chemical and physical properties of Ni-Si-rich ternary alloys. Therefore, scientists have developed numerous processing techniques to offer the possibility of significant breakthroughs in providing better functionality, reliability, and durability of these materials. One of the common techniques to enhance or modify properties of the engineering materials is additional alloying with different elements. Minor quantities of specific elements serve as a factor for controlling phase formation and structural evolution in metallic alloys by influencing nucleation kinetics and grain boundary interactions [17–22]. In particular, we investigate three novel alloy systems based on Ni₈₀Si₂₀ with minor (5 at.%) additions of Al, Cu, and Zr. The selection of these specific alloying elements was driven by their potential to refine the grain structure and influence precipitation behavior, which can significantly impact microstructure and phase transformations. According to the literature, the use of these elements in particular alloy systems has yielded the following specific results. For instance, Zr has been observed to promote grain refinement [23], leading to strengthening through the refined grain structure [24]. Jiang et al. found that Al exhibits a non-monotonic effect on grain size, initially increasing and then decreasing grain size with increasing content [25]. Al also influences the rate of precipitate formation, increasing precipitation kinetics and effectively refining the as-cast alloy structure [26, 27]. Cu additions, on the other hand, dynamically alter the overall crystallization pro-

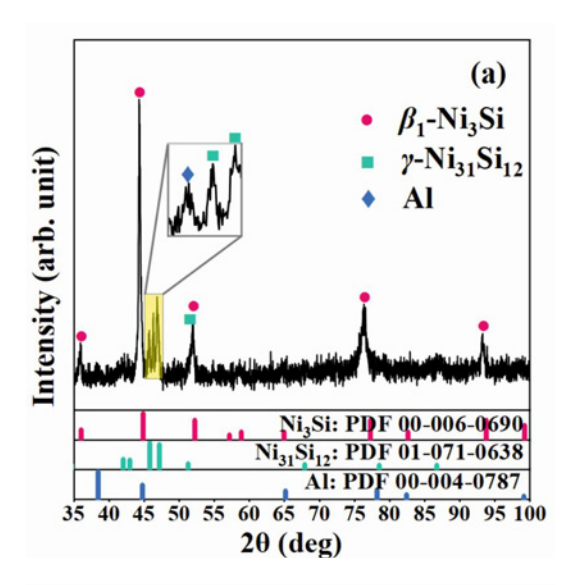
cess [28], with minor Cu facilitating nanocrystallization in Fe-based amorphous alloys [29] and increasing the phase transformation temperatures [30]. Although the individual effects of these elements have been documented in other systems, their combined influence in the specific (Ni₈₀Si₂₀)₉₅M₅ stoichiometry has never been investigated. Furthermore, no previous research has employed the arc melting technique to synthesize these precise ternary compositions. This represents a critical knowledge gap. The present work addresses this gap through the first comprehensive characterization of microstructural, thermal, and magnetic properties of these novel $(Ni_{80}Si_{20})_{95}M_5$ (M = Al, Cu, Zr) ternary alloys produced exclusively via arc melting. Our pioneering findings establish the scientific foundation necessary for designing and optimizing these previously unexplored Ni-Si-rich ternary systems for demanding industrial applications where conventional materials prove inadequate.

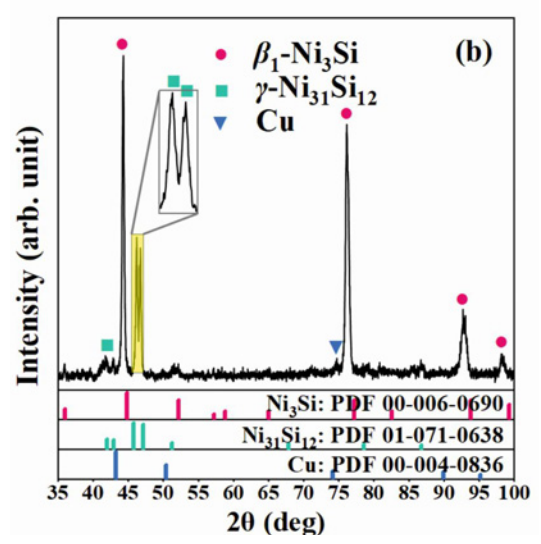
2. Experimental details

Alloys with nominal compositions of (Ni₈₀Si₂₀)₉₅ M_5 (M = Al, Cu, Zr) were prepared by arc melting of certain constituent elements with high purity (> 99.99 pct.) under a vacuum/argon atmosphere. The arc melting process was carried out in a MAM-1 compact arc melter with a water-cooled electrode and a copper crucible plate. Before the melting, the chamber was evacuated to a minimum pressure of $3\times 10^{-5}\,\mathrm{mbar}$ twice and refilled with argon. The major disadvantage of arc-melting is that the lower section of the ingots with direct contact with the watercooled crucible plate may remain solid. Therefore, ingots with a mass of approximately 10 g were flipped and re-melted five times in order to maintain homogeneous composition. Subsequently, the ingots were formed into button shape and subjected to ambient temperature for solidification. All compositions in this paper are given in terms of at.% unless otherwise stated. The crystallographic structure of the alloys was determined at room temperature by X-ray diffraction (XRD) using a Philips X'pert Pro diffractometer with Cu-K α ($\lambda = 0.154 \, \mathrm{nm}$) radiation generated at 40 kV and 30 mA. The diffraction angle is varied in the $2\theta = 20^{\circ}-100^{\circ}$ range with a step size of 0.02° and a count time of 1s per step. The peak positions and intensities were compared with the references listed in the International Center for Diffraction Data (ICDD) files in order to identify the phases. The thermal properties of the alloys, including their phase transformation temperatures, melting behavior, and thermal stability, were investigated using a combination of differential scanning calorimetry (DSC, Perkin-Elmer Sapphire) and differential thermal analysis (DTA, Perkin--Elmer Diamond). While DSC provided detailed information within the range of 100-700°C, at a heating rate of 10 °C min⁻¹ under a constant flow of purified nitrogen, Perkin-Elmer Diamond DTA analysis focused on the 700-1200°C region, complementing the DSC data and revealing the alloys' behavior at higher temperatures. This combined approach gave a complete picture of the alloys' thermal characteristics, enabling identification of phase transitions, precise determination of melting points, and evaluation of their overall thermal stability across a broad temperature spectrum. The morphological properties of the alloys were studied using a scanning electron microscope (SEM, ZEISS EVO LS10) at an acceleration voltage of 25 kV, while their chemical compositions were analyzed through energy-dispersive X-ray spectroscopy (EDX). Vickers micro-hardness testing was chosen for its rapid, minimally destructive, and practical approach to evaluating surface hardness. Measurements were performed using a Shimadzu HMV-2 tester under a 0.98 N load applied for 10 seconds at room temperature, with five indentations taken per alloy to ensure statistical reliability. Magnetic behavior of the alloys is investigated under an external magnetic field in the range of \pm 3 T, at 300 K, using a physical property measurement system (PPMS) with a vibrating sample magnetometer (VSM) head.

3. Results and discussion

X-ray diffraction (XRD) analysis was conducted on finely polished samples using Cu K α radiation (λ = 1.5406 Å) at room temperature to determine the crystal structures of constituent phases. Resulting diffraction patterns were compared to the ICDD reference database with respect to their peak positions and intensities, as illustrated in Fig. 1. The XRD patterns of the alloys show diffraction peaks corresponding to two nickel silicide phases, namely β_1 -Ni₃Si (ICDD--PDF # 00-006-0690) and γ -Ni₃₁Si₁₂ (ICDD-PDF #01-071-0638). These intermetallic compounds with almost identical peak positions were carefully differentiated with the help of relative peak intensities, and no other nickel silicide phases or other crystalline impurities were detected. However, it should be noted that phase identification can be particularly challenging due to indistinguishable diffraction patterns [31]. For example, Suryanarayana reported that NiSi₂ and Si have crystal structures and lattice parameters very close to each other [12]. Mullis et al. also echo a similar comment that both α -Ni and β_1 -Ni₃Si have the same cubic structure with the lattice constant "a" being 3.5244 and 3.5050 Å, respectively [32, 33]. As depicted in Fig. 1, the alloys displayed characteristic diffraction peaks, with the most intense reflection occurring at $2\theta = 44.3^{\circ}$, corresponding to the (111) plane of the cubic β_1 -Ni₃Si phase (space group: Pm-3m, No. 221).





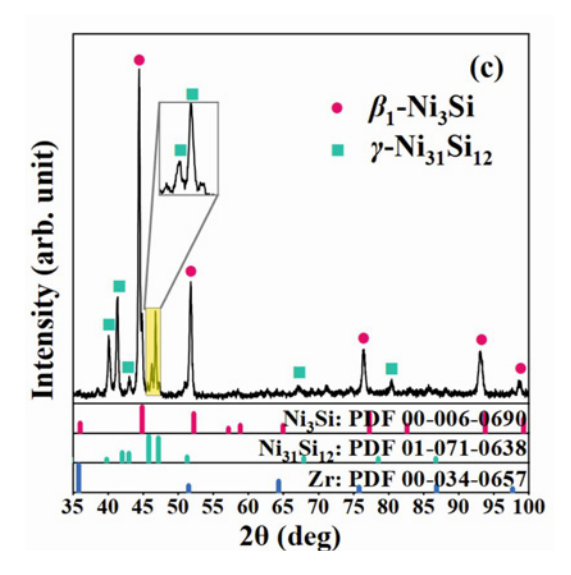


Fig. 1. X-ray diffraction patterns of the alloys: (a) $(Ni_{80}Si_{20})_{95}Al_5$, (b) $(Ni_{80}Si_{20})_{95}Cu_5$, and (c) $(Ni_{80}Si_{20})_{95}$

Table 1.	Crystallographic	parameters	of the	alloys	obtained	with	two	${\rm different}$	${\bf software}$	packages	using	the	${\bf Scherrer}$
					equation	n							

Alloy	$2\theta_{111} \ (^{\circ})$	HighScore Plus FWHM (°)	OriginPro, Voigt Fit FWHM (°)	d-spacing (Å)	$D_{111} \text{ (nm)}$
$(Ni_{80}Si_{20})_{95}Cu_5$	44.22	0.30	0.33	2.04	28.51
$(Ni_{80}Si_{20})_{95}Al_5$	44.29	0.25	0.29	2.04	33.10
$(Ni_{80}Si_{20})_{95}Zr_5$	44.37	0.22	0.28	2.04	36.21

Despite variations in peak intensities due to the presence of a third element, the (111) reflection near $2\theta =$ 44.3° remains the dominant characteristic peak, confirming the cubic crystallization symmetry and indicating that the β_1 -Ni₃Si phase predominates in all samples. This observation suggests that the β_1 -Ni₃Si phase, linked to the highest-intensity peak at $2\theta =$ 44.3°, is the most stable phase within our ternary system under the studied conditions. There are also XRD peaks denoting the presence of Al and Cu elements, yet the peak intensities are very low due to their low amount, which is hardly detectable considering the limitations of XRD. In contrast, no distinct peaks associated with Zr were detected, suggesting that Zr atoms are either fully dissolved in the Ni-Si matrix or present in highly dispersed form below the detection threshold. These observations indicate that the third alloying elements are either dissolved into the matrix or finely distributed along the grain boundaries. This distribution likely contributes to lattice distortion, thereby hindering dislocation motion and enhancing the mechanical strength of the alloys, as supported by previous studies [34, 35]. In addition, while examining the diffraction patterns of the (Ni₈₀Si₂₀)₉₅Cu₅ alloy, we observed that the peak intensity at approximately $2\theta = 76^{\circ}$ is significantly higher compared to the corresponding peaks in the other alloys. Since Si exhibits a strong reflection from the (220) plane at this angle, we initially considered this discrepancy to be related to a silicon-rich metallic phase. However, our phase analysis confirms the presence of only β_1 -Ni₃Si and γ -Ni₃₁Si₁₂ across all three alloys. Notably, the addition of 5 at.% Cu appears to have played a key role in enhancing the intensity of this peak, suggesting that Cu either promotes the formation of the β_1 -Ni₃Si phase, leading to an increased phase fraction, or influences its crystallographic orientation, thereby affecting diffraction intensity. A similar effect was reported by Rodriguez et al. [36], who attributed an increased peak intensity to the presence of a metal-rich silicide phase, specifically an orthorhombic δ -Ni₂Si-like phase labeled as δ -(Ni-Co)₂Si in their Co-containing system. Figure 1 also provides additional information on peak assignments based on the ICDD reference database, ensuring precise phase identification. To enhance clarity, certain peak regions have been magnified, allowing for a more detailed visualization of overlapping

peaks and minor phase contributions. This zoomed-in analysis highlights subtle differences in peak intensity and positioning, further confirming the presence of β_1 -Ni₃Si and γ -Ni₃₁Si₁₂ as the primary phases. Apart from that, all of the diffraction peaks detected are in good agreement with previous reports.

Another key feature of XRD patterns is the estimation of the average crystallite size. As we know, there is an inverse relationship between peak width and crystallite size. The Scherrer equation quantitatively describes the relationship:

$$D_{\rm hlk} = \kappa \lambda / \beta_{\rm hkl} \cos \theta, \tag{1}$$

with the following parameters: average crystallite size in direction perpendicular to the lattice planes $(D_{\rm hkl})$, hkl are the Miller indices of the planes being analyzed; numerical factor frequently referred to as the crystallite-shape factor (κ) ; wavelength of the X-rays (λ) ; width (full-width at half-maximum, "fwhm") of the X-ray diffraction peak in radians $(\beta_{\rm hkl})$; Bragg angle (θ) [37, 38].

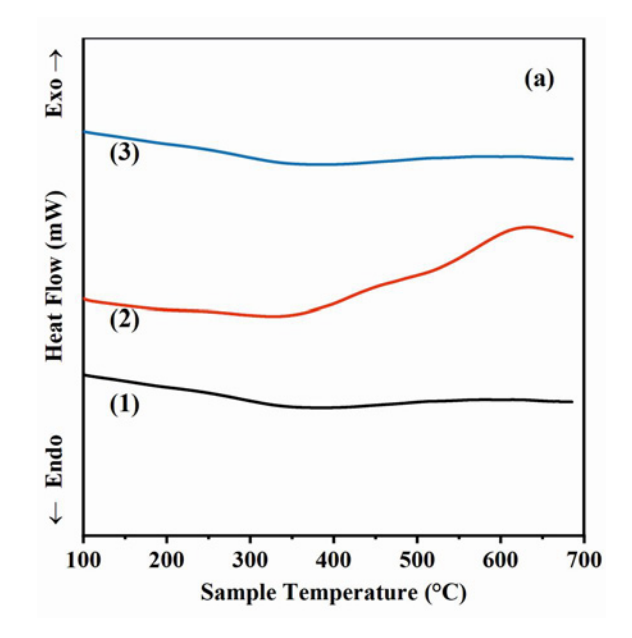
The average crystallite size was determined using the Scherrer equation with the help of both *OriginPro* (OriginLab Corporation, Northampton, MA, USA) and *HighScore Plus software* [39]. The most intense diffraction peaks at the (111) plane were selected, and corresponding fwhm values were calculated by fitting them to a Voigt function, which is a convolution of Gaussian and Lorentzian functions.

The fitting results obtained from both software packages demonstrate excellent agreement, validating the reliability of our crystallographic analysis. The calculated average crystallite sizes for the arc-melted alloys, as presented in Table 1, are 28.51, 33.10, and 36.21 nm for the Cu, Al, and Zr-doped compositions, respectively.

These results indicate that the crystallite size of the studied alloys is significantly influenced by the third alloying element. This is likely due to the direct effect of atomic radii on interatomic spacing, which determines the lattice structure of a crystal. The samples analyzed in this study included Cu, Al, and Zr as alloying elements, each with varying atomic radii. Cu has a smaller atomic radius of 0.128 nm compared to Al (0.143 nm) and Zr (0.159 nm). The XRD analysis results indicate that the alloy containing Zr, which has

Reaction	Composition of	the respective	e phases at.% Si	Temperature (°C)	Reactive type	
$L \rightleftharpoons (Ni) + \beta_3$	21.4	15.8	25.0	1143	Eutectic	
$(Ni) + \beta_2 \rightleftharpoons \beta_1$	14.7	25.1	23.7	1035	Peritectoid	
$L + \gamma \rightleftharpoons \beta_3$	22	27.9	25.2	1170	Peritectic	

Table 2. Thermal reactions in Ni-Si system [44]



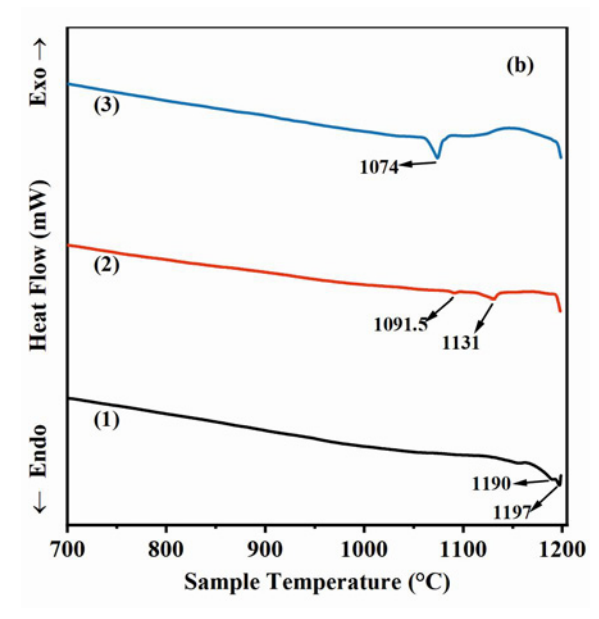


Fig. 2. DSC (a) and DTA (b) traces of the alloys: (1) $(Ni_{80}Si_{20})_{95}Al_5$, (2) $(Ni_{80}Si_{20})_{95}Cu_5$, and (3) $(Ni_{80}Si_{20})_{95}$

the largest atomic radius among the alloying elements, also had the largest average crystallite size.

Figure 2 shows the typical DSC (left) and DTA

(right) traces of the arc-melted alloys. As shown in the DSC traces, all alloys, from $100\,^{\circ}\mathrm{C}$ onwards, follow a similar trend and show no indication of melting or glass transition. This suggests that no phase transformations are occurring within $100-700\,^{\circ}\mathrm{C}$, and all the alloys are thermally stable. Previous findings are also consistent with this result [6,40,41]. Another point is that Al has the lowest melting point of $660\,^{\circ}\mathrm{C}$ in our ternary systems, which can be easily traced by DSC due to the strongest tendency to evaporate during arcmelting, yet no endothermic reactions were observed. A possible explanation for this result may be causally associated with low local concentration due to a relatively small amount of Al $(5\,\mathrm{at.\%})$ and Al dissolving in other components [42].

Despite providing useful information about the thermal transitions, one of the major drawbacks of DSC is the limited temperature range. In order to overcome this limitation and further investigate the thermal properties at higher temperatures, we refer to the DTA. As can be seen from Fig. 2, the same trend without any significant endothermic peaks holds up to 1000°C during DTA measurements. However, depending on the third alloying element (Al, Cu, or Zr at 5 at.%), single or double endothermic peaks between 1074 and $1197\,^{\circ}\!\mathrm{C}$ are observed for our alloys. The absence of endothermic peaks for phases containing the additional elements may be attributed to their local concentrations not being high enough [43]. Based on the Ni-Si phase diagram in Fig. 3, these thermal events correspond to interactions between three anticipated phases: α -Ni solid solution, β_1 -Ni₃Si, and γ -Ni₃₁Si₁₂.

The specific thermal reactions associated with these phases, according to the Ni-Si phase diagram, are summarized in Table 2.

By referring to the Ni-Si phase diagram reported by Nash [44] and Baker [45] in Fig. 3, the observed DTA peaks indicate that melting is occurring between the crystalline mixtures of high-strength β_1 -Ni₃Si and γ -Ni₃Si₁₂ phases. Similar results were reported among the samples containing Ni-Si elements with relatively close compositions and ratios [6, 40, 46]. Among the alloying additions, Al increases the transformation temperatures more than Cu and Zr, indicating that 5 at.% Al stabilizes high-temperature phases, as seen in thermal events at 1190 and 1197 °C. In contrast, Zr induces the most significant reduction in transformation temperatures. Overall, the observed

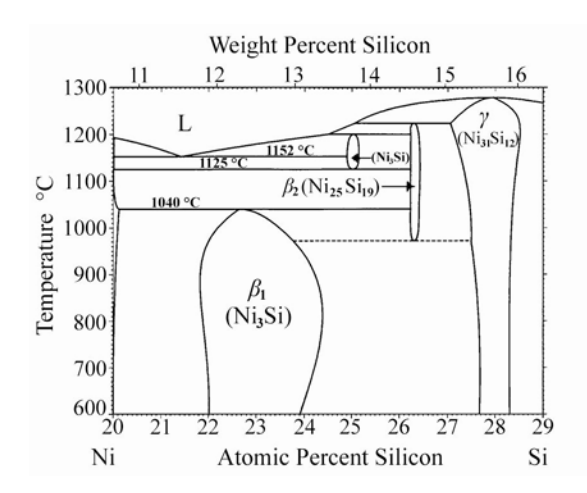
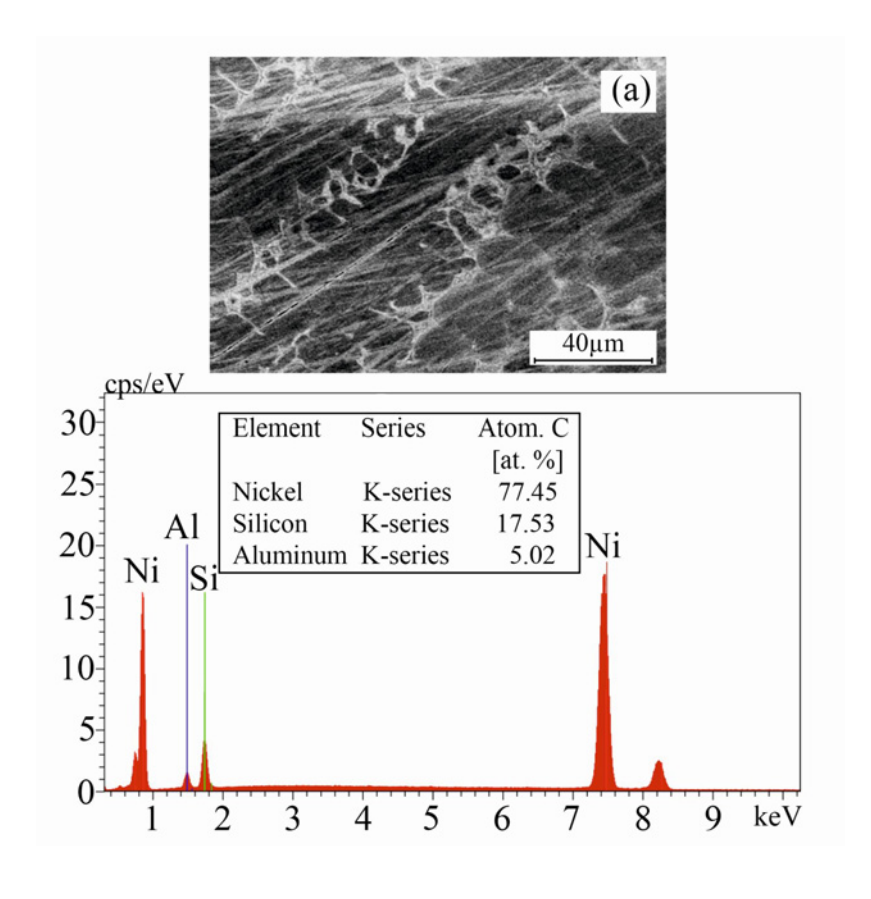


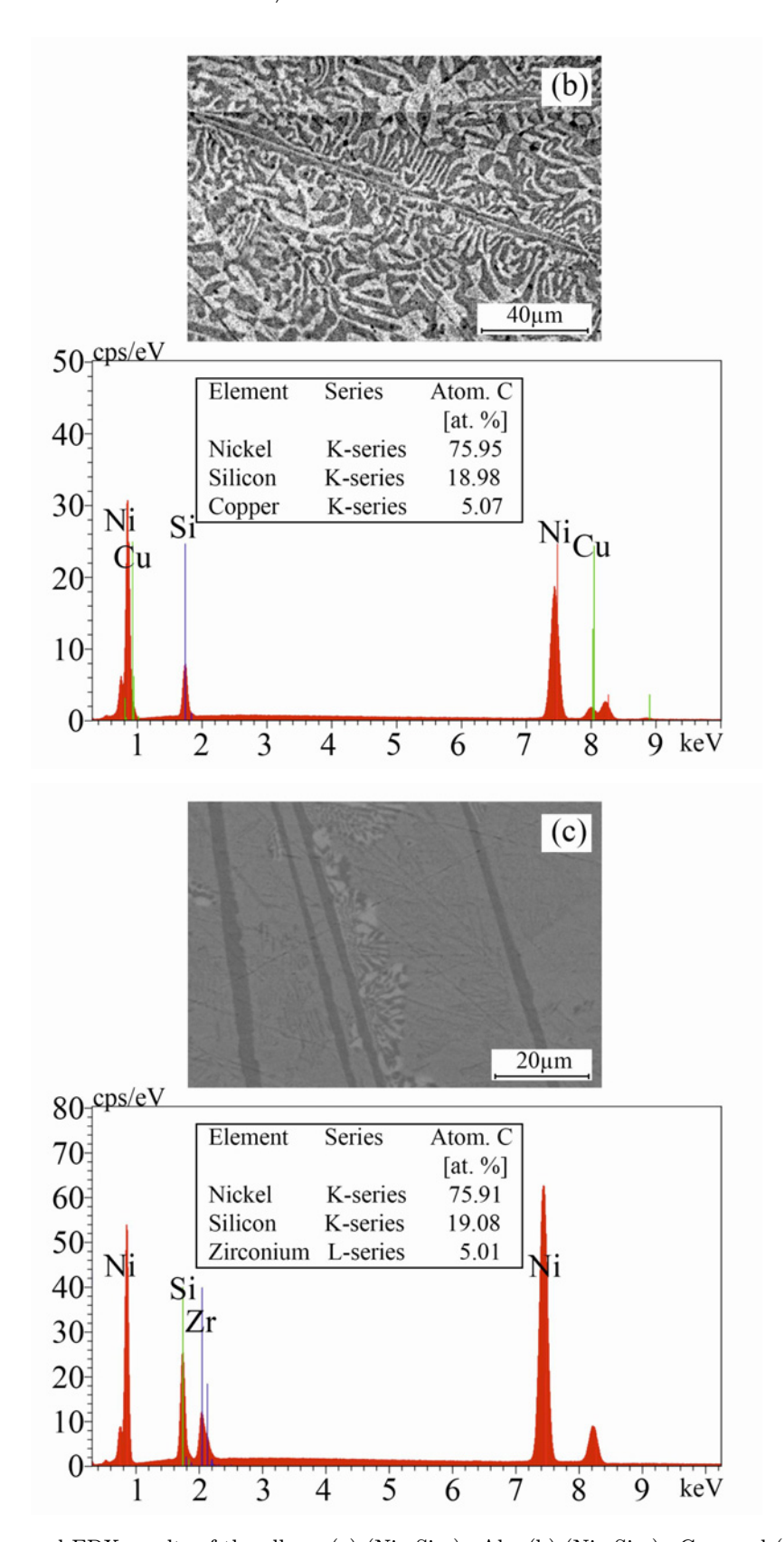
Fig. 3. Ni-Si binary phase diagram [44].

transitions highlight the critical role of ternary additions in altering the phase stability and melting behavior of Ni-Si-based ternary alloys.

As stated in the previous results, the introduction of the third alloying element has a pronounced impact on the microstructure of the alloys. Consequently, these effects on the microstructure give rise to substantial alterations in the morphology of the alloys. Therefore, the morphological properties were as-

sessed by SEM and EDX as shown in Fig. 4. In the SEM analysis, we observed characteristic features of planar, cellular, and dendritic growth patterns. The dark gray phases signify relatively Si-rich solid solutions, while the light gray phases denote relatively Ni-rich intermediate phases. When incorporating 5 at.% Al into the alloy, we observe the surface morphology exhibiting a cellular dendritic growth pattern. On the other hand, with the introduction of Cu and Zr, we observe columnar dendritic growth and planar growth, respectively. Furthermore, the addition of copper results in the development of columnar dendritic structures with secondary and tertiary dendrite arms. Despite notable progress, the underlying factors driving the transition from cells to dendrites remain unclear. The opaqueness and high melting temperature of the samples pose challenges in maintaining precise control over the solidification process [47, 48]. However, we believe that variations in alloy composition can lead to different degrees of undercooling, which, in turn, impact the kinetics of solidification and, therefore, the growth pattern. Both the XRD and SEM-EDX results confirm that the alloys are composed of intermetallic phases, and compositional homogeneity is achieved, with values very close to the nominal compositions. In addition, we not only observed distinct peaks corresponding to the starting elements of Ni, Si, Al, Cu, and Zr in the EDX spectra analysis but also found no





 $Fig. \ 4. \ SEM \ images \ and \ EDX \ results \ of \ the \ alloys: (a) \ (Ni_{80}Si_{20})_{95}Al_5, (b) \ (Ni_{80}Si_{20})_{95}Cu_5, \ and \ (c) \ (Ni_{80}Si_{20})_{95}Zr_5.$

evidence of impurity peaks. This observation further suggests that minimal loss of the solute elements dur-

ing solidification and synthesis procedures has been achieved.

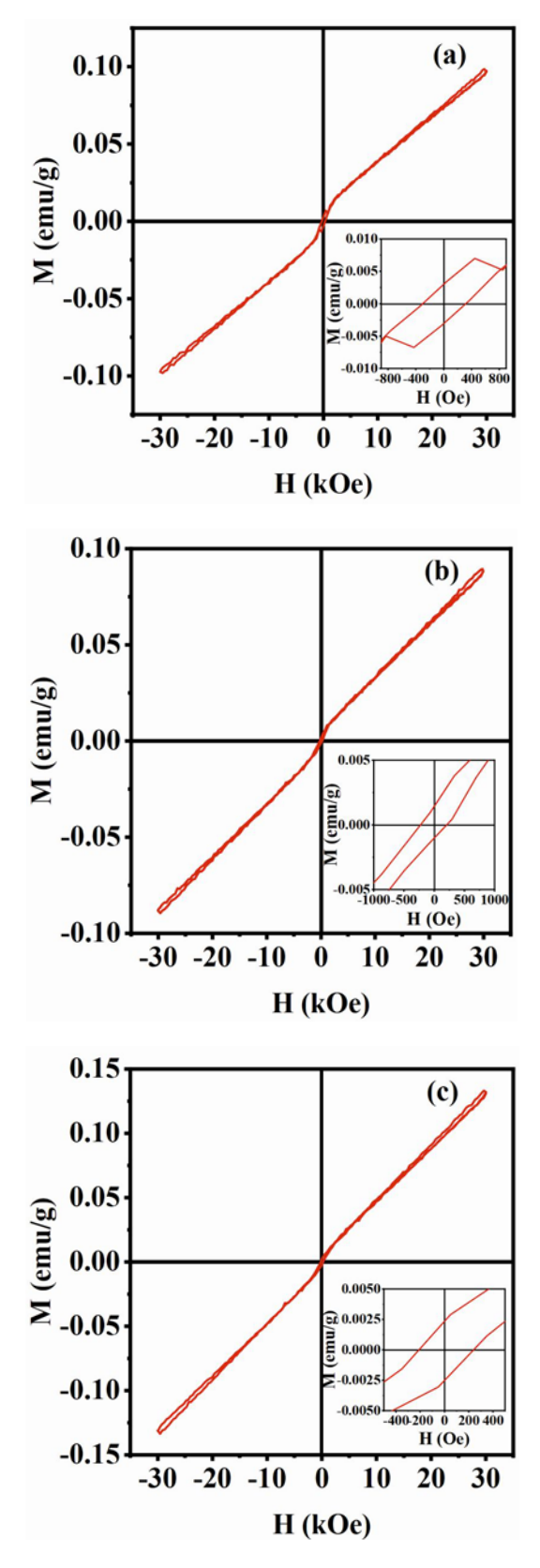


Fig. 5. Magnetization vs. magnetic field (M-H) measurements of the alloys at 300 K: (a) $(Ni_{80}Si_{20})_{95}Al_5$, (b) $(Ni_{80}Si_{20})_{95}Cu_5$, and (c) $(Ni_{80}Si_{20})_{95}Zr_5$.

Table 3. Magnetic properties of the alloys at 300 K

Alloys	$H_{\rm c}$ (Oe)	$M_{\rm r}~({\rm emu~g}^{-1})$
$(Ni_{80}Si_{20})_{95}Cu_5$	219	0.0015
$(Ni_{80}Si_{20})_{95}Al_5$	307	0.003
$(Ni_{80}Si_{20})_{95}Zr_5$	225	0.0023

Magnetic behavior of the alloys is investigated under an external magnetic field in the range of \pm 3 T, at 300 K. Figure 5 illustrates the resulting magnetic hysteresis loops, which provide distinct magnetic responses of each alloy. Remanent magnetization (M_r) and coercivity (H_c) values obtained from the M-H curves are also listed in Table 3. As shown in Table 3, the $(Ni_{80}Si_{20})_{95}Al_5$ alloy exhibits a coercivity of 307 Oe and a remanent magnetization of 0.003 emu g⁻¹, while the $(Ni_{80}Si_{20})_{95}Cu_5$ alloy has a coercivity of 219 Oe and a remanent magnetization of 0.0015 emu g⁻¹. Additionally, the $(Ni_{80}Si_{20})_{95}Zr_5$ alloy shows a coercivity of 225 Oe and a remanent magnetization of 0.0023 emu g⁻¹.

When we refer to Table 3, we can see that there are no recorded values for saturation magnetization $(M_{\rm s})$ regarding the alloys. The absence of saturation magnetization (M_s) values can be attributed to several factors, including certain conditions that prevent the alloys from reaching saturation under the applied field conditions: (i) the presence of non-ferromagnetic elements such as silicon (diamagnetic), copper (diamagnetic), aluminum (paramagnetic), and zirconium (paramagnetic) can dilute the overall magnetization, resulting in a low or absent M_s . Additionally, the introduction of these elements may have induced defects or disturbances in the lattice structure, hindering the alignment of magnetic moments and leading to a paramagnetic-like response; (ii) different phase formations can also influence the magnetic response [40, 49, 50]; (iii) as Mourdikoudis discussed decreasing crystallite size below the critical radius limit can result in lack of saturation magnetization in the materials [51]. Furthermore, Alnasir and Rana have also mentioned that effects such as surface spin disorder, spin-canting, and thermal fluctuations could contribute to the result [52, 53].

Another result that has caught our attention is that the alloys with 5 at.% Al, Zr, and Cu have coercivity values of 307, 225, and 219 Oe, respectively. Notably, among these alloys, those containing 5 at.% Al and Zr exhibit larger crystallite sizes compared to Cu, as indicated by XRD results. The increase in coercivity with increasing crystallite size can be attributed to the phenomenon observed when magnetic domains remain below the critical size (single domain), as demonstrated in Fig. 6. This also confirms the relationship

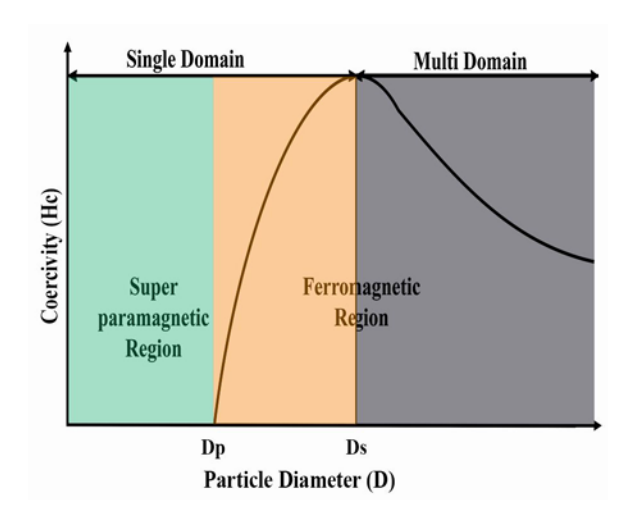


Fig. 6. Size dependence of coercivity; $D_{\rm p}$ represents the particle diameter at the superparamagnetic regime, while $D_{\rm s}$ denotes the particle diameter at the transition from the single to the multi-domain regime [54–56].

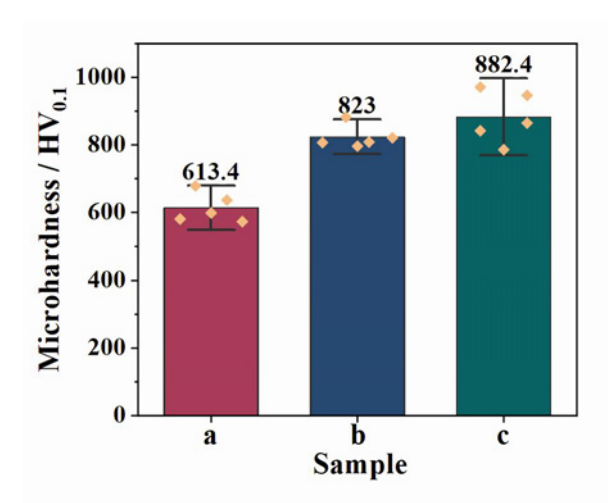


Fig. 7. Vickers micro-hardness values of the alloys: (a) $(Ni_{80}Si_{20})_{95}Al_5$, (b) $(Ni_{80}Si_{20})_{95}Cu_5$, and (c) $(Ni_{80}Si_{20})_{95}Zr_5$.

between the critical atomic radius and saturation magnetization mentioned in our previous comment.

Overall, the absence of saturation magnetization, combined with very low remanent magnetization and low coercivity values, indicates that the alloys exhibit paramagnetic behavior.

The Vickers micro-hardness values, as given in Fig. 7, demonstrate significant variations among the ternary alloys. The $(Ni_{80}Si_{20})_{95}Zr_5$ alloy exhibits the highest hardness value, reaching 882.4 ± 76.5 HV, followed by the $(Ni_{80}Si_{20})_{95}Cu_5$ alloy with a value of 823.0 ± 34.2 HV and the $(Ni_{80}Si_{20})_{95}Al_5$ alloy, which has the lowest hardness at 613.4 ± 43.8 HV. This trend can be directly correlated with the observed microstructural differences, as evidenced in

Fig. 4. The Zr-containing alloy displays a planar growth pattern, contrasting with the cellular dendritic and columnar dendritic structures of the Al- and Cu-containing alloys, respectively. The more uniform microstructure in the Zr-containing alloy, with fewer defect accumulation sites, likely contributes to its superior hardness by promoting a consistent phase distribution and minimizing localized stress concentrations [57, 58]. Furthermore, the larger atomic radius of Zr compared to Al and Cu may introduce additional lattice strain, further impeding dislocation motion and enhancing hardness [59–61].

4. Conclusions

In this study, we conducted a thorough investigation into the structural, thermal, magnetic, and morphological properties of ternary Ni-Si-based alloys with 5 at.% additions of Al, Cu, or Zr. Through X-ray diffraction (XRD) analysis, we successfully confirmed the dominance of the cubic β_1 -Ni₃Si phase (space group: Pm-3m, No. 221) and the presence of γ -Ni₃₁Si₁₂ phase, with no detectable impurities. The estimation of average crystallite size using the Scherrer equation revealed dependences on the third alloying element, indicating variations in lattice structure. Notably, (Ni₈₀Si₂₀)₉₅Zr₅ alloy demonstrated the largest average crystallite size of 36.21 nm. Thermal analysis using differential scanning calorimetry (DSC) confirmed the thermal stability of the alloys below 680°C, while differential thermal analysis (DTA) identified melting events occurring between 1074 and 1197℃, suggesting phase transitions between the expected phases at elevated temperatures. The addition of Al increased transformation temperatures, while Zr reduced them. The investigation into the magnetic properties of the alloys revealed two key points. Firstly, the ternary alloys exhibit low remanent magnetization ($\sim 0.002 \,\mathrm{emu}\,\mathrm{g}^{-1}$) and moderate coercivity (219-307 Oe), suggesting weak permanent magnetism and paramagnetic-like behavior. (Ni₈₀Si₂₀)₉₅Al₅ possesses the highest coercivity (307 Oe), while $(Ni_{80}Si_{20})_{95}Cu_5$ has the lowest (219 Oe). Secondly, the absence of saturation magnetization is attributed to non-ferromagnetic elements diluting the magnetization and potentially disrupting the lattice structure, along with potential contributions from factors like phase formations, small crystallite size, and surface spin disorder. Scanning electron microscopy (SEM) and energy-dispersive X-ray spectroscopy (EDX) analysis revealed distinct morphologies for each alloy: cellular dendritic with Ni-Si-Al, columnar dendritic with Ni-Si-Cu, and planar growth with Ni-Si-Zr. Notably, the alloys achieved both compositional homogeneity and minimal loss of solute elements. Finally, Vickers micro-hardness measurements further highlighted the alloys' diverse characteristics, $(Ni_{80}Si_{20})_{95}Zr_5$ alloy demonstrating the highest hardness at $882.4 \pm 76.5\,\mathrm{HV}$, followed by the $(Ni_{80}Si_{20})_{95}Cu_5$ at $823.0 \pm 34.2\,\mathrm{HV}$, and the $(Ni_{80}Si_{20})_{95}Al_5$ at $613.4 \pm 43.8\,\mathrm{HV}$. Overall, this study successfully demonstrates the impact of third alloying elements (5 at.% Al, Zr, Cu) on the structural, thermal, magnetic, and morphological properties of Ni-Si-rich ternary alloys, while also laying the groundwork for further understanding and optimizing their performance in various applications.

Acknowledgements

The authors gratefully acknowledge that the present publication is an output from a research project (Project no. 2015/3-60D) funded by Kahramanmaras Sutcu Imam University. We also extend our thanks to Dr. Hakan Yaykasli for technical assistance with XRD and SEM.

References

- T. M. Pollock, Alloy design for aircraft engines, Nature Materials 15 (2016) 809–15.
 https://doi.org/10.1038/nmat4709
- K. Lu, The Future of metals, Science 328 (2010) 319–320. https://doi.org/10.1126/science.1185866
- [3] T. M. Pollock, S. Tin, Nickel-based superalloys for advanced turbine engines: chemistry, microstructure and properties, Journal of Propulsion and Power 22 (2006) 361–374. https://doi.org/10.2514/1.18239
- [4] W. Wang, H. Kang, Z. Chen, Z. Chen, C. Zou, R. Li, G. Yin, T. Wang, Effects of Cr and Zr additions on microstructure and properties of Cu-Ni-Si alloys, Materials Science and Engineering A 673 (2016) 378–390. https://doi.org/10.1016/j.msea.2016.07.021.
- [5] E. Çadirli, D. M. Herlach, E. Davydov, Microstructural, mechanical, electrical and thermal characterization of arc-melted Ni-Si and Co-Si alloys, Journal of Non-Crystalline Solids 356 (2010) 1735–1741. https://doi.org/10.1016/j.jnoncrysol.2010.06.005
- [6] E. Karaköse, M. Keskin, Investigation of microstructural, mechanical and thermal properties of rapidly solidified Ni-7wt.% Si alloy, Materials Science and Engineering A 553 (2012) 181–191. https://doi.org/10.1016/j.msea.2012.06.013
- [7] A. V. Nikiforov, I. M. Petrushina, E. Christensen, A. L. Tomás-García, N. J. Bjerrum, Corrosion behaviour of construction materials for high temperature steam electrolysers, International Journal of Hydrogen Energy 36 (2011) 111–119. https://doi.org/10.1016/j.ijhydene.2010.09.023
- [8] J. Xu, T. Shoji, C. Jang, The effects of dissolved hydrogen on the corrosion behavior of Alloy 182 in simulated primary water, Corrosion Science 97 (2015) 115–125. https://doi.org/10.1016/j.corsci.2015.04.021
- [9] D. Upadhyay, M. A. Panchal, R. S. Dubey, V. K. Srivastava, Corrosion of alloys used in dentistry: A review, Materials Science and Engineering A 432 (2006) 1–11. https://doi.org/10.1016/j.msea.2006.05.003

- [10] D. Mareci, R. Chelariu, S. Iacoban, C. Munteanu, G. Bolat, D. Sutiman, The estimation of localized corrosion behavior of Ni-based dental alloys using electrochemical techniques, Journal of Materials Engineering and Performance 21 (2012) 1431–1439. https://doi.org/10.1007/s11665-011-0014-1
- [11] C. R. M. Afonso, K. Martinez-Orozco, V. Amigó, C. A. Della Rovere, J. E. Spinelli, C. S. Kiminami, Characterization, corrosion resistance and hardness of rapidly solidified Ni-Nb alloys, Journal of Alloys and Compounds 829 (2020) 154529. https://doi.org/10.1016/j.jallcom.2020.154529
- [12] A. A. Al-Joubori, C. Suryanarayana, Synthesis of stable and metastable phases in the Ni-Si system by mechanical alloying, Powder Technology 302 (2016) 8–14. https://doi.org/10.1016/j.powtec.2016.08.033
- [13] K. Omuro, H. Miura, Amorphization of M-Si (M = Ni, Co, Mo, Mn, and Cr) powders by ball milling using revolution-step-like-decreasing mode, Applied Physics Letters 60 (1992) 1433–1435. https://doi.org/10.1063/1.107313
- [14] M.-S. Park, S. Rajendran, Y.-M. Kang, K.-S. Han, Y.-S. Han, J.-Y. Lee, Si-Ni alloy-graphite composite synthesized by arc-melting and high-energy mechanical milling for use as an anode in lithium-ion batteries, Journal of Power Sources 158 (2006) 650–653. https://doi.org/10.1016/j.jpowsour.2005.08.052
- [15] T. Takasugi, H. Kawai, Y. Kaneno, The effect of Cr addition on mechanical and chemical properties of Ni₃Si alloys, Materials Science and Engineering A 329–331 (2002) 446–454. https://doi.org/10.1016/s0921-5093(01)01619-7
- [16] U. Böyük, S. Engin, N. Maraşli, Microstructural characterization of unidirectional solidified eutectic Al-Si-Ni alloy, Materials Characterization 62 (2011) 844–851. https://doi.org/10.1016/j.matchar.2011.05.010
- [17] P. Chowdhury, H. Sehitoglu, W. Abuzaid, H. J. Maier, Mechanical response of low stacking fault energy Co-Ni alloys – Continuum, mesoscopic and atomic level treatments, International Journal of Plasticity 71 (2015) 32–61. https://doi.org/10.1016/j.ijplas.2015.04.003
- [18] Z.-H. Chen, J.-H. Chen, A review: Hot topics on magnesium technology in China, Frontiers of Materials Science in China 2 (2008) 1–8. https://doi.org/10.1007/s11706-008-0001-0
- [19] C. Li, Y. Wu, H. Li, Y. Wu, X. Liu, Effect of Ni on eutectic structural evolution in hypereutectic Al-Mg₂Si cast alloys, Materials Science and Engineering A 528 (2010) 573–577. https://doi.org/10.1016/j.msea.2010.09.056
- [20] A. M. Russell, Ductility in intermetallic compounds, Advanced Engineering Materials 5 (2003) 629–639. https://doi.org/10.1002/adem.200310074
- [21] S. Zhu, G. Xie, F. Qin, X. Wang, A. Inoue, Effect of minor Sn additions on the formation and properties of TiCuZrPd bulk glassy alloy, Materials Transactions 53 (2012) 500–503. https://doi.org/10.2320/matertrans.M2011281
- [22] X. M. Li, M. J. Starink, Identification and analysis of intermetallic phases in overaged Zr-containing and Cr-containing Al-Zn-Mg-Cu alloys, Journal of Alloys and Compounds 509 (2011) 471–476. https://doi.org/10.1016/j.jallcom.2010.09.064

- [23] W. Yuan, Z. Liang, Effect of Zr addition on properties of Al-Mg-Si aluminum alloy used for all aluminum alloy conductor, Materials & Design 32 (2011) 4195–4200. https://doi.org/10.1016/j.matdes.2011.04.034
- [24] H. Kaya, A. Aker, Effect of alloying elements and growth rates on microstructure and mechanical properties in the directionally solidified Al-Si-X alloys, Journal of Alloys and Compounds 694 (2017) 145–154. https://doi.org/10.1016/j.jallcom.2016.09.199
- [25] Z. Jiang, B. Jiang, Y. Zeng, J. Dai, F. Pan, Role of Al modification on the microstructure and mechanical properties of as-cast Mg-6Ce alloys, Materials Science and Engineering A 645 (2015) 57–64. https://doi.org/10.1016/j.msea.2015.08.002
- [26] Q. Lei, Z. Li, C. Dai, J. Wang, X. Chen, J. M. Xie, W.W. Yang, D. L. Chen, Effect of aluminum on microstructure and property of Cu-Ni-Si alloys, Materials Science and Engineering A 572 (2013) 65–74. https://doi.org/10.1016/j.msea.2013.02.024
- [27] M. Gholami, J. Vesely, I. Altenberger, H. A. Kuhn, M. Janecek, M. Wollmann, L. Wagner, Effects of microstructure on mechanical properties of CuNiSi alloys, Journal of Alloys and Compounds 696 (2017) 201–212.

https://doi.org/10.1016/j.jallcom.2016.11.233

- [28] H. Y. Jung, S. Yi, Effect of Cu addition on nanocrystallization behaviors and magnetic properties of the Fe76.5-xC6.0Si3.3B5.5P8.7Cux (x = 0–3 at.%) bulk metallic glass, Journal of Alloys and Compounds 561 (2013) 76–81.
 - $\underline{\text{https://doi.org/10.1016/j.jallcom.2013.01.165}}$
- [29] H. Y. Jung, M. Stoica, S. Yi, D. H. Kim, J. Eckert, Preparation of cast-iron-based nanocrystalline alloy with Cu and Nb addition, Intermetallics 69 (2016) 54– 61. https://doi.org/10.1016/j.intermet.2015.10.014
- [30] C. L. Tan, G. F. Dong, L. Gao, J. H. Sui, Z. Y. Gao, W. Cai, Microstructure, martensitic transformation and mechanical properties of Ni50Mn30Ga20-xCux ferromagnetic shape memory alloys, Journal of Alloys and Compounds 538 (2012) 1–4. https://doi.org/10.1016/j.jallcom.2012.05.121
- [31] C. F. Holder, R. E. Schaak, Tutorial on powder X-ray diffraction for characterizing nanoscale materials, ACS Nano 13 (2019) 7359–7365. https://doi.org/10.1021/acsnano.9b05157
- [32] L. Cao, R. F. Cochrane, A. M. Mullis, Solidification morphology and phase selection in drop-tube processed Ni-Fe-Si intermetallics, Intermetallics 60 (2015) 33–44.

https://doi.org/10.1016/j.intermet.2015.01.006

- [33] L. Cao, R. F. Cochrane, A. M. Mullis, Microstructural evolution and phase formation in rapidly solidified Ni-25.3 at. pct Si alloy, Metallurgical and Materials Transactions A 46 (2015) 4705–4715. https://doi.org/10.1007/s11661-015-3070-6
- [34] Y. Ye, X. Li, K. Hu, S. Qu, Y. Li, Effects of alloy composition on microstructure and mechanical properties of iron-based materials fabricated by ball milling and spark plasma sintering, Metallurgical and Materials Transactions A 46 (2014) 476–487. https://doi.org/10.1007/s11661-014-2597-2
- [35] X. Zhang, Y. Zhang, B. Tian, K. Song, P. Liu, Y. Jia, X. Chen, J. An, Z. Zhao, Y. Liu, A. A.

- Volinsky, X. Li, T. Yin, Review of nano-phase effects in high strength and conductivity copper alloys, Nanotechnology Reviews 8 (2019) 383–395. https://doi.org/10.1515/ntrev-2019-0034
- [36] P. Rodriguez, F. Deprat, C. Sésé, S. Zhiou, S. Favier, C. Fenouillet-Béranger, T. Luo, D. Mangelinck, P. Gergaud, F. Nemouchi, Phase formation sequence and cobalt behavior in the Ni_{0.9}Co_{0.1} system during the thin film solid-state formation, Microelectronic Engineering 200 (2018) 19–25. https://doi.org/10.1016/j.mee.2018.08.006
- [37] A. L. Patterson, The Scherrer formula for X-Ray particle size determination, Physical Review 56 (1939) 978– 982. https://doi.org/10.1103/PhysRev.56.978
- [38] P. Scherrer, Determination of the size and internal structure of colloid particles using X-rays, Nachr. Ges. Wiss. Gottingen, Math.-Phys. Kl. 2 (1918) 98–100. (in German)
- [39] T. Degen, M. Sadki, E. Bron, U. König, G. Nénert, The HighScore suite, Powder Diffraction 29 (2014) S13-S18. https://doi.org/10.1017/s0885715614000840
- [40] M. Gogebakan, C. Kursun, K. O. Gunduz, M. Tarakci, Y. Gencer, Microstructural and mechanical properties of binary Ni-Si eutectic alloys, Journal of Alloys and Compounds 643 (2015) S219–S225. https://doi.org/10.1016/j.jallcom.2014.12.058
- [41] E. Karaköse, M. Keskin, Microstructure evolution and mechanical properties of intermetallic Ni-xSi (x = 5, 10, 15, 20) alloys, Journal of Alloys and Compounds 528 (2012) 63–69. https://doi.org/10.1016/j.jallcom.2012.02.165
- [42] M. Şahin, E. Çadirli, Mechanical, electrical, and thermal properties of the directionally solidified Bi-Zn-Al ternary eutectic alloy, International Journal of Minerals, Metallurgy, and Materials 21 (2014) 999–1008. https://doi.org/10.1007/s12613-014-1001-y
- [43] J. Barrirero, C. Pauly, M. Engstler, J. Ghanbaja, N. Ghafoor, J. Li, P. Schumacher, M. Odén, F. Mücklich, Eutectic modification by ternary compound cluster formation in Al-Si alloys, Scientific Reports 9 (2019) 5506. https://doi.org/10.1038/s41598-019-41919-2
- [44] P. Nash, A. Nash, The Ni-Si (Nickel-Silicon) system, Bulletin of Alloy Phase Diagrams 8 (1987) 6–14. https://doi.org/10.1007/BF02868885
- [45] H. Baker, Alloy Phase Diagrams. in: ASM International (Ed.), ASM Handbook, ASM International, Ohio, 1992, p. 318. ISBN: 0-87170-377-7
- [46] A. T. Dutra, S. Milenkovic, C. S. Kiminami, A. M. Santino, M. C. Gonçalves, R. Caram, Microstructure and metastable phase formation in a rapidly solidified Ni-Si eutectic alloy using a melt-spinning technique, Journal of Alloys and Compounds 381 (2004) 72–76. https://doi.org/10.1016/j.jallcom.2004.02.059
- [47] D. A. Porter, K. E. Easterling, M. Y. Sherif, Phase Transformations in Metals and Alloys, third ed., CRC Press, Florida, 2009. https://doi.org/10.1201/9781439883570
- [48] W. Losert, B. Q. Shi, H. Z. Cummins, Evolution of dendritic patterns during alloy solidification: Onset of the initial instability, Proceedings of the National Academy of Sciences 95 (1998) 431–438. https://doi.org/10.1073/pnas.95.2.431
- [49] B. Avar, M. Gogebakan, S. Ozcan, S. Kerli, Structural, mechanical and magnetic properties of Fe – 40

- at.% Al powders during mechanical alloying, Journal of the Korean Physical Society 65 (2014) 664-670. https://doi.org/10.3938/jkps.65.664
- [50] C. Kursun, M. Gogebakan, E. Uludag, M. S. Bozgeyik, F. S. Uludag, Structural, electrical and magnetic properties of Nd-A-CoO₃ (A = Sr, Ca) Perovskite powders by mechanical alloying, Scientific Reports 8 (2018) 13083. https://doi.org/10.1038/s41598-018-31458-7
- [51] S. Mourdikoudis, K. Simeonidis, A. Vilalta-Clemente, F. Tuna, I. Tsiaoussis, M. Angelakeris, C. Dendrinou-Samara, O. Kalogirou, Controlling the crystal structure of Ni nanoparticles by the use of alkylamines, Journal of Magnetism and Magnetic Materials 321 (2009) 2723–2728.
 - https://doi.org/10.1016/j.jmmm.2009.03.076
- [52] M. H. Alnasir, M. Y. Khan, W. B. Ali, M. Z. Ansar, S. Manzoor, Magnetic and hyperthermia properties of $\mathrm{Ni}_{1-x}\mathrm{Cu}_x$ nanoparticles coated with oleic acid and silica prepared via sol-gel method, Applied Physics A 125 (2019) 532.
 - https://doi.org/10.1007/s00339-019-2820-5
- [53] G. Rana, P. Dhiman, A. Kumar, D.-V. N. Vo, G. Sharma, S. Sharma, M. Naushad, Recent advances on nickel nano-ferrite: A review on processing techniques, properties and diverse applications, Chemical Engineering Research and Design 175 (2021) 182–208. https://doi.org/10.1016/j.cherd.2021.08.040
- [54] G. C. Hadjipanayis, Nanophase hard magnets, Journal of Magnetism and Magnetic Materials 200 (1999) 373–391. https://doi.org/10.1016/S0304-8853(99)00430-8
- [55] D. C. Jiles, Recent advances and future directions in magnetic materials, Acta Materialia 51 (2003) 5907– 5939. https://doi.org/10.1016/j.actamat.2003.08.011

- [56] J. Sung Lee, J. Myung Cha, H. Young Yoon, J.-K. Lee, Y. Keun Kim, Magnetic multi-granule nanoclusters: A model system that exhibits universal size effect of magnetic coercivity, Scientific Reports 5 (2015) 12135. https://doi.org/10.1038/srep12135
- [57] A. Školáková, P. Novák, D. Vojtěch, T. F. Kubatík, Microstructure and mechanical properties of Al-Si-Fe-X alloys, Materials & Design 107 (2016) 491–502. https://doi.org/10.1016/j.matdes.2016.06.069
- [58] H. Eskalen, M. Aslan, H. Yaykaşlı, M. Gögebakan, Synthesis and characterization of Co-B-Fe-Ti nanosized alloyed powders, International Journal of Materials Research 112 (2021) 35–41. https://doi.org/10.1515/ijmr-2020-7704
- [59] M. Ahmed, T. Fouzder, A. Sharif, A. K. Gain, Y. C. Chan, Influence of Ag micro-particle additions on the microstructure, hardness and tensile properties of Sn-9Zn binary eutectic solder alloy, Microelectronics Reliability 50 (2010) 1134–1141. https://doi.org/10.1016/j.microrel.2010.03.017
- [60] B. He, X. Cheng, J. Li, X.-J. Tian, H.-M. Wang, Effect of laser surface remelting and low temperature aging treatments on microstructures and surface properties of Ti-55511 alloy, Surface and Coatings Technology 316 (2017) 104–112. https://doi.org/10.1016/j.surfcoat.2016.11.097
- [61] B. Fu, K. Feng, Z. Li, Study on the effect of Cu addition on the microstructure and properties of NiTi alloy fabricated by laser cladding, Materials Letters 220 (2018) 148–151.

https://doi.org/10.1016/j.matlet.2018.03.030